AGU PUBLICATIONS

Geophysical Research Letters

RESEARCH LETTER
10.1002/2015GL067183

Key Points:
- Coseismic EM signals were observed during the 2004 Parkfield earthquake
- The coseismic EM signals were modeled based on electrokinetic theory
- The synthetic electric fields explain the observed data

Supporting Information:
- Texts S1–S3 and Tables S1–S3

Correspondence to:
Y. Gao,
gaoyx@hfut.edu.cn

Citation:
Gao, Y., J. M. Harris, J. Wen, Y. Huang, C. Twardzik, X. Chen, and H. Hu (2016), Modeling of the coseismic electromagnetic fields observed during the 2004 M_w 6.0 Parkfield earthquake, *Geophys. Res. Lett.*, *43*, 620–627, doi:10.1002/2015GL067183.

Received 25 NOV 2015
Accepted 3 JAN 2016
Accepted article online 6 JAN 2016
Published online 22 JAN 2016

Modeling of the coseismic electromagnetic fields observed during the 2004 M_w 6.0 Parkfield earthquake

Yongxin Gao[1,2], Jerry M. Harris[2], Jian Wen[3], Yihe Huang[2], Cedric Twardzik[4], Xiaofei Chen[3], and Hengshan Hu[5]

[1]School of Civil Engineering, Hefei University of Technology, Hefei, China, [2]Department of Geophysics, Stanford University, Stanford, California, USA, [3]School of Earth and Space Sciences, University of Science and Technology of China, Hefei, China, [4]Department of Earth Science, University of California, Santa Barbara, California, USA, [5]Department of Astronautics and Mechanics, Harbin Institute of Technology, Harbin, China

Abstract The coseismic electromagnetic signals observed during the 2004 M_w 6 Parkfield earthquake are simulated using electrokinetic theory. By using a finite fault source model obtained via kinematic inversion, we calculate the electric and magnetic responses to the earthquake rupture. The result shows that the synthetic electric signals agree with the observed data for both amplitude and wave shape, especially for early portions of the records (first 9 s) after the earthquake, supporting the electrokinetic effect as the reasonable mechanism for the generation of the coseismic electric fields. More work is needed to explain the magnetic fields and the later portions of the electric fields. Analysis shows that the coseismic electromagnetic (EM) signals are sensitive to both the material properties at the location of the EM sensors and the electrochemical heterogeneity in the vicinity of the EM sensors and can be used to characterize the underground electrochemical properties.

1. Introduction

On 28 September 2004 a M_w 6 earthquake took place on the San Andreas Fault at Parkfield, California. It is the so-called long-awaited earthquake as it was expected to happen between 1983 and 1993 [*Bakun and McEvilly*, 1984] but finally occurred 10 years later. Before this earthquake, in 1995 U.C. Berkeley researchers installed two electromagnetic (EM) monitoring sites on the San Andreas Fault (http://quake.geo.berkeley.edu/bdsn/em.overview.html, last accessed 23 November 2015), namely, PKD and SAO (red triangles in Figure 1a), for the purpose of monitoring possible changes in electric and magnetic fields prior to earthquakes. The PKD site is located only 20.9 km from the epicenter of the 2004 Parkfield earthquake (red star in Figure 1a) and equipped with seismic and EM sensors, both of which worked normally on the day of the 2004 Parkfield earthquake and continuously recorded seismic and EM signals before, during, and after onset of the earthquake. No obvious changes above noise level can be found in either the electric or magnetic fields before the initiation of the earthquake. But during and after the earthquake significant coseismic EM signals were recorded along with the three-component accelerations (Figure 2). The electric and magnetic signals appeared simultaneously with the seismic arrivals and looked similar in shape to the seismic acceleration. Similar coseismic EM signals were also observed during some other earthquake events (e.g., 1998 M_w 5.1 San Juan Bautista earthquake on the San Andreas Fault [*Karakelian et al.*, 2002], 1999 İzmit earthquake [*Matsushima et al.*, 2002], and aftershocks following the 2008 M_s 8.0 Wenchuan earthquake [*Tang et al.*, 2010; *Huang*, 2011; *Gao et al.*, 2014]), but the mechanisms to generate such EM signals are still not clearly understood.

Several mechanisms have been proposed to explain the generation of the earthquake-induced EM signals, including the piezoelectric effect [*Huang*, 2002], the piezomagnetic effect [*Okubo et al.*, 2011; *Yamazaki*, 2011], the seismic dynamo effect (or motional induction effect) [*Matsushima et al.*, 2002; *Gao et al.*, 2014], and the electrokinetic effect [*Pride*, 1994; *Gao and Hu*, 2010; *Ren et al.*, 2015]. Among these mechanisms, we examine the electrokinetic effect, which arises from the existence of the electric double layer in a fluid-saturated medium and has attracted a lot of attention. Theoretical studies based on the electrokinetic effect [*Pride*, 1994] were conducted to simulate both the waveforms and amplitudes of the EM response to an earthquake assuming a double-couple point source [*Gao and Hu*, 2010; *Ren et al.*, 2010; *Gao et al.*, 2013a, 2013b] or a finite fault rupture [*Hu and Gao*, 2011; *Ren et al.*, 2012, 2015]. By adjusting the source parameters and by choosing suitable parameters for earth materials, the synthetic EM signals are found to have comparable

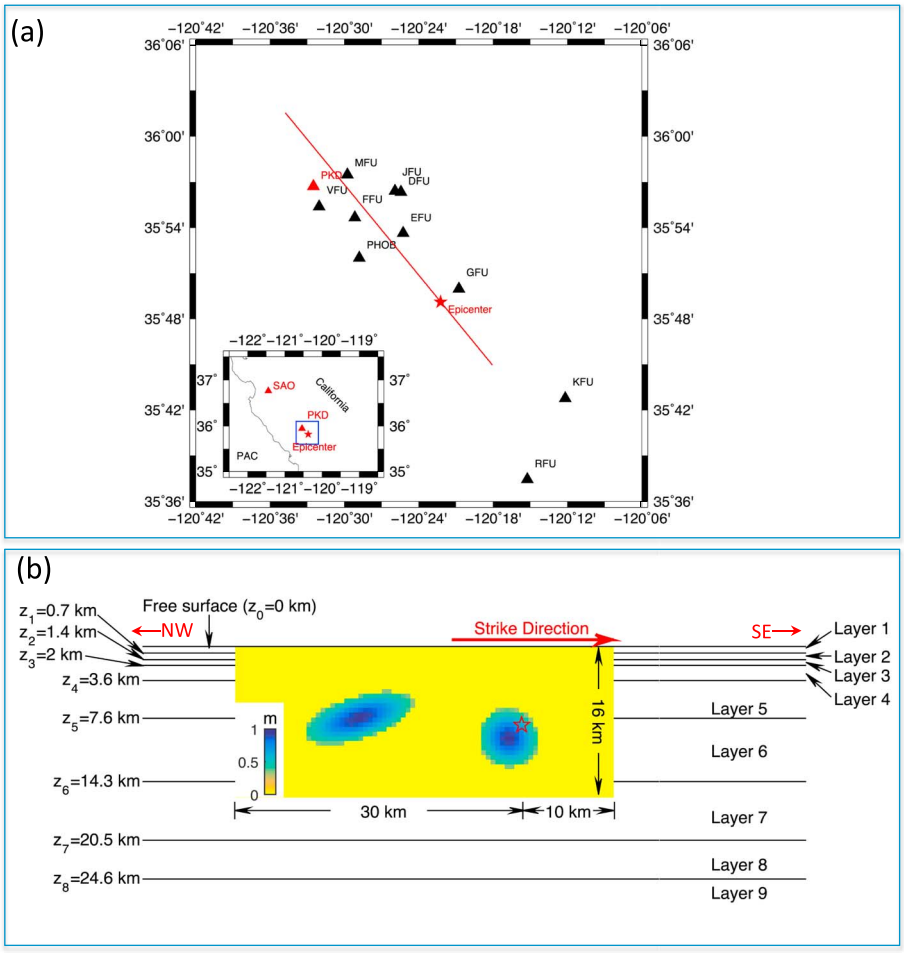

Figure 1. (a) Locations of the epicenter of the 2004 Parkfield earthquake (red star) and stations. The two red triangles indicate the PKD and SAO EM monitoring sites whose locations are (35.9452°N, 120.5416°W) and (36.7640°N, 121.4472°W), respectively. The 10 black triangles represent the digital strong motion stations, of which the seismic data are used for the inversion of source parameters by *Twardzik et al.* [2012]. The latitude and longitude of each strong motion station can be found in *Liu et al.* [2006]. The red straight line represents the modeled fault rupture. (b) Nine-layer model for the subsurface material of the northeast side of the fault. The parameters of each layer are listed in Table S1. The yellow rectangle represents the modeled fault plane of the 2004 Parkfield earthquake, which is 40 km long along strike and 16 km wide along dip. The slip distribution on the fault plane consists of two distinct ellipses and shows no slip in the top 5 km. The color denotes the slip amplitude. Rupture time distribution on the fault plane can be found in *Twardzik et al.* [2012]. The red star at a depth of 8.26 km represents the hypocenter. The symbols "NW" and "SE" in red indicate the northwest and southeast directions, respectively.

amplitudes with the observed data. However, these studies did not investigate the real earthquake events or use the real source rupture model [e.g., *Liu et al.* [2006]]. To study the earthquake-induced EM phenomenon, it is very important to simulate the EM signals observed during real earthquake event by using the real source model and compare the synthetic waveforms to the observed data.

The 2004 Parkfield earthquake provides an unprecedented opportunity to study observed EM signals. First, the earthquake took place on the San Andreas Fault, along which the velocity structure is known with high resolution [e.g., *Lees and Malin*, 1990; *Michelini and McEvilly*, 1991; *Thurber et al.*, 2003, 2006]. Second, the rupture process of this earthquake is well studied and resolved from kinematic inversions [*Ji et al.*, 2004; *Liu et al.*, 2006; *Kim and Dreger*, 2008; *Twardzik et al.*, 2012], dynamic modeling [*Ma et al.*, 2008], and dynamic inversion [*Twardzik et al.*, 2014]. These previous studies are beneficial for studying the coseismic EM fields generated by the 2004 Parkfield earthquake. In the present article, we simulate the coseismic EM signals on the basis of the electrokinetic theory and compare the calculated waveforms with the observed data. The main goal is to explore whether the electrokinetic effect can explain the observed EM signals.

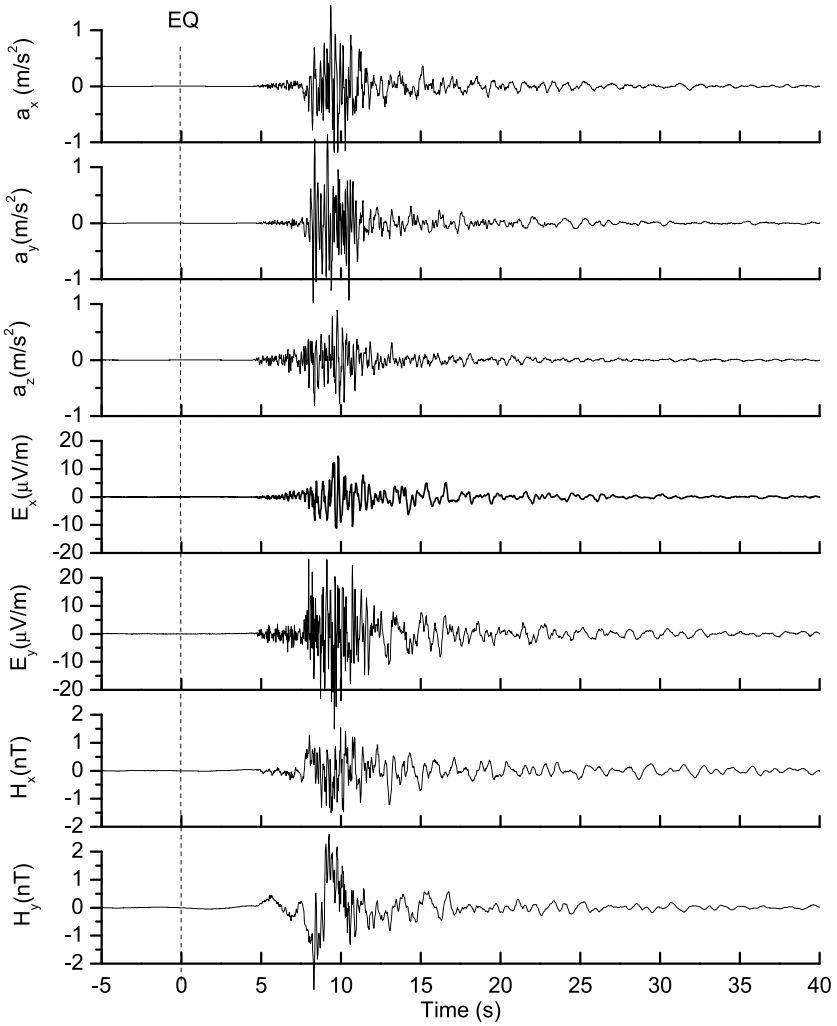

Figure 2. Coseismic EM signals observed at PKD during the 2004 M_W 6 Parkfield earthquake. a_x, a_y, and a_z represent the seismic accelerations. E_x and E_y are the horizontal electric fields. H_x and H_y are the horizontal magnetic fields. The subscripts *x*, *y*, and *z* indicate the geographic north, east, and vertical directions, respectively. The symbol "EQ" indicates the origin time of the earthquake, i.e., $t = 0$ s. In order to remove the effect from long-period wave components, a zero-phase Butterworth high-pass filter with a cutoff frequency of 0.16 Hz is applied to both the seismic and EM signals.

2. Observation

The PKD site (Figure 1a) is equipped with three orthogonal induction coils to measure the time-varying magnetic field (0.0001–20 Hz) and two pairs of electrodes to measure the changes in horizontal electric field (direct current–20 Hz) in the surface plane. It is also equipped with seismic sensors to measure the three orthogonal components of the seismic acceleration. The EM and seismic data are, respectively, recorded at 40 and 80 samples per second, respectively, by a 24 bit Quanterra digital data logger and collected at Berkeley Digital Seismic Network site. The waveform data are archived by Northern California Earthquake Data Center (NCEDC), where one can download the data from the website www.ncedc.org (last accessed 23 November 2015). More detailed information about the installation of the EM instruments can be found in *Kappler* [2008] or the NCEDC website.

Figure 2 shows the waveforms of the seismic accelerations and electric and magnetic fields from 5 s before the origin time of the earthquake to 40 s after. The vertical component of the magnetic field is not displayed in Figure 2 because it is partly clipped due to limitations of the magnetometer. During the 2008 Iwate-Miyagi *M* 7.2 earthquake, corupture magnetic signals from the source arriving earlier than the *P* wave were detected [*Okubo et al.*, 2011]. Unfortunately, no such corupture disturbances can be found in either the electric or magnetic fields immediately after the 2004 Parkfield earthquake rupture started. This might be due to the relatively

smaller magnitude of the 2004 Parkfield earthquake. After the *P* wave arrived, clear coseismic electric and magnetic signals were generated and even stronger signals were produced when the *S* wave arrived. The maximum amplitudes of the electric fields reached the order of 10 μV/m, while those of the magnetic fields were on the order of 1 nT. These EM disturbances were caused by the seismic waves since they returned to noise level after the passing of the seismic waves. Although EM signals were also recorded at the SAO site, which is located 112 km northwest to the earthquake epicenter, here we only study the coseismic EM signals observed at PKD.

3. Procedures for Modeling the EM Signals Based On the Electrokinetic Effect

3.1. Theoretical Basis

We simulate the observed EM signals at PKD based on the electrokinetic effect. To quantitatively describe the electrokinetic effect, we use equations from *Pride* [1994] (referred to hereafter as Pride's equations), which couple the elastodynamic equations depicting elastic wave propagation in fluid-saturated porous media [*Biot*, 1962] and Maxwell equations describing the propagation of the EM waves. The coupling between the seismic and EM wavefields is controlled by the electrokinetic coupling coefficient that can be experimentally measured [e.g., *Jaafar et al*., 2009; *Wang et al*., 2015] or theoretically estimated [e.g., *Pride*, 1994; *Revil et al*., 1999]. Based on Pride's equations, several algorithms were developed to simulate the seismoelectromagnetic wavefields in the unbounded full space and horizontally layered media generated by various sources [e.g., *Pride and Haartsen*, 1996; *Haartsen and Pride*, 1997; *Gao and Hu*, 2009, 2010; *Hu and Gao*, 2011; *Ren et al*., 2012, 2015]. Here we use the method developed by *Hu and Gao* [2011] to simulate the seismic and EM wavefields generated by the 2004 Parkfield earthquake. This method allows us to calculate the seismic and EM responses to a finite fault rupture in a horizontally layered half-space (as shown in Figure 1b). The whole fault plane is divided into a series of subfaults. The wavefield is then calculated for each subfault and finally stacked in order to get the contributions from all of the subfaults. A brief review of this method as well as Pride's equations can be found in Text S1 in the supporting information. To perform the modeling, two important sets of input information are needed, namely, the source model and the subsurface material parameters.

3.2. Source Model

We use the preferred kinematic source model given by *Twardzik et al*. [2012] to simulate the rupture process of the 2004 Parkfield earthquake. Figure 1b shows the modeled fault plane (yellow rectangle) with the slip distribution on it. One can refer to *Twardzik et al*. [2012] for detailed information about the source model as well as the inversion method.

3.3. Parameters of the Subsurface Media for Simulations

To model the electrokinetic phenomenon, Pride's equations require a porous medium model to describe the subsurface material. The following parameters are needed: the elastic moduli *H*, *C*, *M*, and *G*; density ρ; porosity ϕ, permeability κ_0; tortuosity α_∞; fluid density ρ_f; fluid viscosity η; fluid salinity C_0; zeta potential ζ; permittivity ε and conductivity σ_0 of the porous medium; and electrokinetic coupling coefficient L_0. Unfortunately, these parameters are not well known close to the fault. As a consequence, we tried different values for these parameters in order to fit the observed data. However, the specifications of the parameters are not arbitrary. The elastic moduli *H*, *C*, *M*, and *G* and density ρ that mainly control the property of the seismic waves are specified in a way that lets the equivalent *P* and *S* wave velocities be the same as those of a corresponding solid layer of the 1-D velocity structure adapted by *Liu et al*. [2006]. Following *Liu et al*. [2006], we consider different materials for the southwest (SW) and northeast (NE) sides of the fault. Figure 1b illustrates the nine-layer model for the NE material. The other parameters, namely, κ_0, α_∞, ρ_f, η, ε, ϕ, C_0, ζ, σ_0, and L_0 (hereafter referred as the electrochemical parameters), which mainly control the coupling between the seismic waves and EM fields, are chosen to have typical values or values within reasonable range. The specifications of all the parameters are listed in Table S1 of the supporting information. A more detailed discussion on the choice of the parameters can be found in Text S2.

4. Results

Using the procedures mentioned above, we calculate the seismic and EM responses to the rupture process of the 2004 Parkfield earthquake. Because the inversion of the source was made in the frequency range 0.16–1 Hz [*Twardzik et al*., 2012], we only calculate the synthetic signals and band-pass filter the observed data in the same

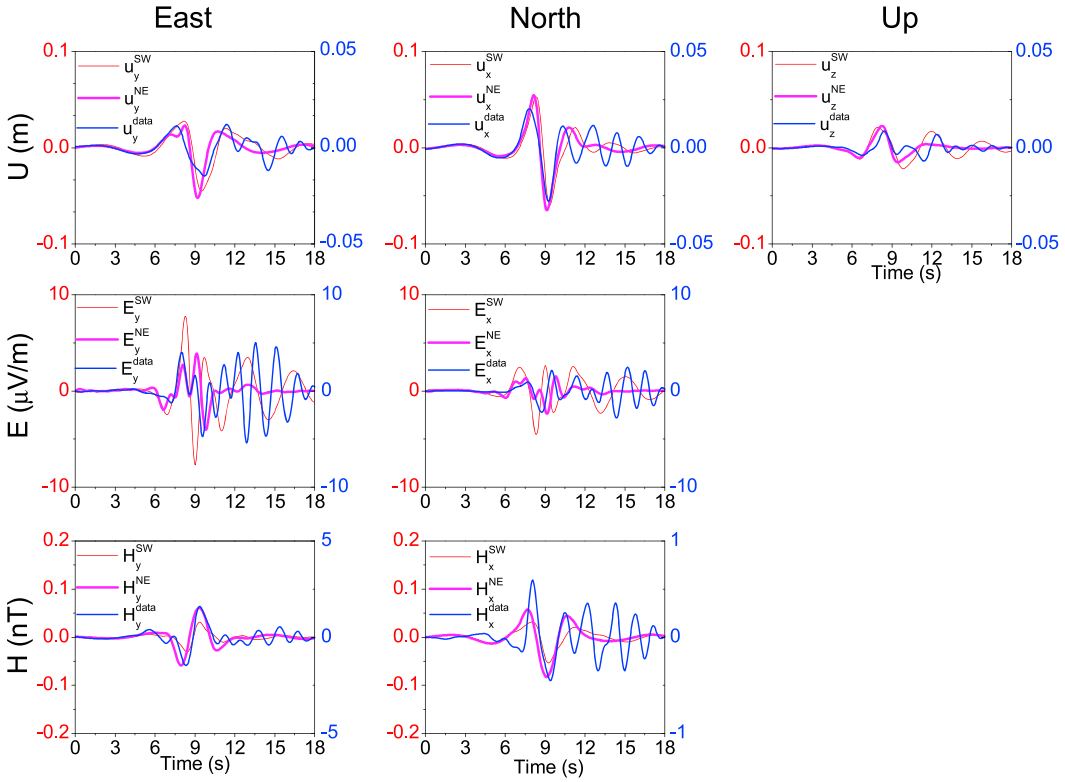

Figure 3. Comparison between the synthetic and observed seismoelectromagnetic fields at PKD. The top three are the seismic displacements, middle two electric fields, and bottom two magnetic fields. The red curves indicate the synthetic signals calculated using the parameters of the southwest material in Table S1, while the pink curves indicate those using the parameters of the northeast material. The blue curves represent the observed data. For each subplot, the left axis in red shows the amplitudes of the synthetic signals, while the right axis in blue shows those of the observed data, and $t = 0$ s indicates the origin time of the earthquake.

frequency range. Figure 3 shows the comparison between the synthetic and observed seismoelectromagnetic wavefields at PKD. The observed displacement is obtained by integrating twice the acceleration data shown in Figure 2. We calculate the signals using both the SW (red curves) and NE (pink curves) materials listed in Table S1. The purpose is to study the effect of the velocity structure on the synthetic EM fields and to investigate which material produces better synthetic EM fields.

As can be seen from the top three subplots of Figure 3, the synthetic displacements calculated by using the SW and NE materials fit the observed displacements well in the phase although their amplitudes are about two times larger than observed displacement (note that the scales for the left and right axes are different). During the inversion of the source model by *Twardzik et al.* [2012] only the seismic data from the 10 digital strong motion stations (black triangles in Figure 1a) were used, while the seismic data at PKD were not used. The good match between the synthetic and observed displacements at PKD shows the reliability of the source model.

The synthetic electric fields at PKD were also simulated by using the NE and SW materials (middle two subplots in Figure 3). It can be seen that the amplitudes of the synthetic electric fields resulting from both the SW (E_x^{SW}, E_y^{SW}) and NE (E_x^{NE}, E_y^{NE}) materials are several μV/m, agreeing with the observed data (E_x^{data}, E_y^{data}). For the north component in 0–8.5 s, E_x^{SW} and E_x^{NE} exhibit similar waveforms as well as the same polarity, and both of them match the observed signal E_x^{data}. The east component of the electric fields (E_y^{NE} and E_y^{SW}) also fit the observed signal (E_y^{data}) in the same time range. In particular E_y^{NE} matches E_y^{data} a little better because at time $t = 9$ s both E_y^{NE} and E_y^{data} have a crest, while E_y^{SW} has a trough. In the later portion of the records (8.5–18 s), the SW and NE synthetic waveforms show large differences, and neither of them matches the observed wave shape.

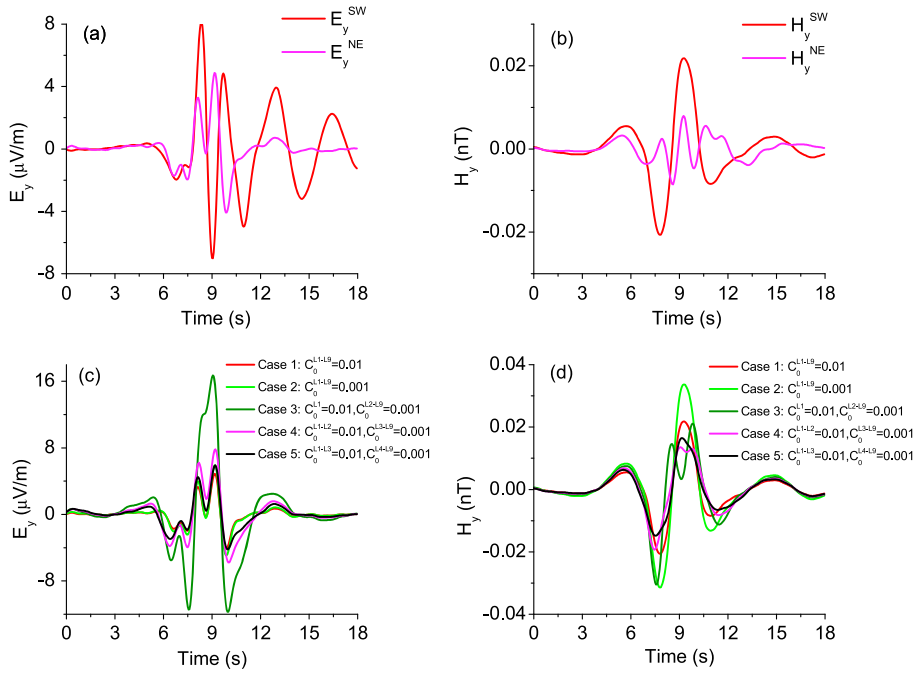

Figure 4. (a) Electric and (b) magnetic fields at PKD that are calculated by using two materials with SW and NE velocity structures (composed of *H*, *C*, *M*, and *G* and density ρ), respectively. The electrochemical parameters (κ_0, α_∞, ρ_f, η, ε, ϕ, C_0, ζ, σ_0, and L_0) have uniform values through all the layers of the two materials listed in Table S2. (c) Electric and (d) magnetic fields calculated by using five cases of salinity distributions among the nine layers of the NE material. ζ, σ_0, and L_0 are set to change with salinity C_0 (see Table S3), while the other parameters *H*, *C*, *M*, *G*, ρ, κ_0, α_∞, ρ_f, η, ε, and ϕ are kept unchanged as listed in Table S2. In the legends, C_0^{Li} represents the salinity of the *i*th layer and the unit mol/L is omitted. The electric field of Case 2 has been scaled by a factor of 0.1 for the convenience of comparison.

The bottom two subplots of Figure 3 compare the synthetic and observed magnetic fields. The synthetic magnetic signals capture the main features of the observed data in the early portions of the records (0–11 s), especially for the east component, but they have much smaller amplitudes (less than 0.1 nT) than the observed data (more than 1 nT). Note that the magnetic sensors likely moved during the passage of seismic waves, inducing additional magnetic signals. However, the removal of the motion-induced magnetic signals was not attempted in this study. Therefore, we only discuss the coseismic electric signal below.

5. Discussion

Unlike the coseismic magnetic fields, the study by *Ujihara et al.* [2004] indicates that the coseismic electric fields are not due to the movement of the cables but reflect the response due to electric current flowing in the ground. Thus, the mismatch between the synthetic and observed electric signals that we observe in the later portions of records may arise from several causes.

First, the EM fields depend on the subsurface materials, and the material parameters used in our simulations may be not accurate enough. Figures 4a and 4b show the EM fields at PKD calculated by using two materials that have SW and NE velocity structures, respectively. The other electrochemical parameters are set to be uniform for all the layers of the two materials (see Table S2). The EM fields calculated from the two materials are different, implying that they are sensitive to the velocity structure. Figures 4c and 4d show the influence of the salinity on the EM signals at the PKD site. We have considered five cases of distributions of the salinity C_0 among the nine layers of the NE material (see Table S3). In Cases 1 and 2, the salinities are specified with uniform values through all the layers. In Case 3, 4, and 5 contrasts in salinity are introduced across the interfaces between Layers 1 and 2, Layers 2 and 3, and Layers 3 and 4. The salinities are set to be 0.01 mol/L above the interfaces and 0.001 mol/L below. We can see that the EM signals resulting from each of these five cases are different, indicating that the coseismic EM signals are also sensitive to the electrochemical parameters, i.e., parameters that are not well known.

The second reason for the disagreement between the later portions of the synthetic and observed electric signals may arise from limitations of the source model. For example, the fault zone waves were not modeled in the source model, and we can also observe the mismatch between the later portions of the synthetic and observed displacements in Figure 3. Besides, the synthetic EM signals were limited to the low frequency range 0.16–1 Hz, while the observed seismic and EM data contain components of higher frequencies (Figure 2). Therefore, to get a better understanding of the coseismic EM signals, a higher-resolution source model is required to model the higher frequency components of the seismic and EM signals.

Another possible reason for disagreement may be due to the fact that other mechanisms such as the motional induction effect [*Gao et al*., 2014] also contribute to the generation of the coseismic EM signals while we only simulate the electrokinetic effect. Combining the EM signals resulting from different mechanisms to explain the observed EM data is a good target for future research.

By studying the medium effects on the coseismic EM fields, we have found two important phenomena looking at Figures 4c and 4d. The first one is that the electric field of Case 2 (green line) is about 10 times stronger than that of Case 1 (red line). Note that the electric field of Case 2 has been scaled by a factor of 0.1 for the convenience of comparison. The magnetic field of Case 2 is also larger than that of Case 1. Since the EM fields are recorded at the free surface (i.e., in Layer 1), such amplitude difference indicates that the coseismic EM fields depend on the salinity at the station location. This agrees with the results obtained by *Gao* [2010] and *Huang et al*. [2015].

The second observed phenomenon is that the EM fields also depend on the materials below Layer 1. For example, between Cases 1 and 3 the salinity of Layer 1 is kept the same, while those of Layers 2 to 9 are changed. We see that the electric field of Case 3 (olivaceous line) differs from that of Case 1 in both the amplitude and wave shape. Such difference is somewhat unexpected because in an isotropic and homogeneous full space the coseismic EM signals accompanying the body *P* and *S* waves depend on the medium property at the location of the EM sensor [*Garambois and Dietrich*, *200*1; *Gao and Hu*, 2010]. We realize that in a bounded model the existence of the interfaces may affect the coseismic EM fields as well. The slow compressional wave generated at the interface between Layers 1 and 2 may contribute significantly to the generation of the EM fields since the distance from the EM sensor to the interface is small (only 0.7 km in Case 3) and the frequencies are low (0.16–1 Hz). Because there is a large contrast in salinity across the interface between Layers 1 and 2 in Case 3 while no such contrast exists in Case 1, a stronger slow compressional wave is generated at the interface in Case 3. If the distance from the EM sensor to the interface of salinity discontinuity becomes larger (i.e., 1.4 km in Case 4 and 2.0 km in Case 5), the effect of the slow compressional wave becomes weaker due to its high attenuation. Therefore, the EM fields of Cases 4 (pink line) and 5 (black line) come close to that of Case 1. These five cases of simulations indicate that the coseismic EM fields depend not only on the material properties at the location of the EM sensors but also on the contrast in electrochemical parameters at interfaces near the EM sensor. This suggests that the coseismic EM signals could be an indicator of underground electrochemical heterogeneity.

6. Conclusions

We simulate the coseismic EM signals observed during the 2004 Parkfield earthquake using the electrokinetic effect. The forward modeling is performed on the basis of Pride's equations, and both seismic and EM responses to the earthquake rupture are evaluated. The result shows that the synthetic coseismic electric fields agree with the observed data not only in the amplitude but also in the wave shape for the early portions of the records, suggesting that the coseismic electric fields are likely to be caused by the electrokinetic effect. However, more work is needed in order to reproduce the later portions of the observed data, including the possibility of using more accurate parameters for the subsurface material and a source model with higher resolution. Contributions from other mechanisms (e.g., the motional induction effect) to the generation of the coseismic electric field also need to be considered. The synthetic magnetic fields show similar waveforms to the observed data in the early portions of the records but have weaker amplitude. Because the motion of the magnetic sensors caused by the seismic waves could produce a change of magnetic field, such effect should be removed from the observed magnetic signals in the future to explain the coseismic magnetic signals.

Acknowledgments
This work is supported by the National Natural Science Foundation of China (grants 41204039 and 41474038) and the Fundamental Research Funds for the Central Universities, China (grant WK2080000055). Waveform data, metadata, or data products for this study were accessed through the Northern California Earthquake Data Center (NCEDC), doi:10.7932/NCEDC. We thank Professor Simon Klemperer, Wei Wang, and Miao Zhang for their help in data processing. We also thank the two reviewers for their constructive comments.

References

Bakun, W. H., and T. V. McEvilly (1984), Recurrence models and Parkfield, California, Earthquakes, *J. Geophys. Res.*, *89*(B5), 3051–3058.
Biot, M. A. (1962), Mechanics of deformation and acoustic propagation in porous media, *J. Appl. Phys.*, *33*(4), 1482–1498.
Gao, Y. (2010), Simulation of earthquake-induced electromagnetic wavefield due to the electrokinetic effect, PhD thesis, Harbin Institute of Technology, Harbin, China.
Gao, Y., and H. Hu (2009), Numerical simulation and analysis of seismoelectromagnetic wave fields excited by a point source in layered porous media, *Chin. J. Geophys.-Chin. Ed.*, *52*(8), 2093–2104.
Gao, Y., and H. Hu (2010), Seismoelectromagnetic waves radiated by a double couple source in a saturated porous medium, *Geophys. J. Int.*, *181*(2), 873–896.
Gao, Y., X. Chen, H. Hu, and J. Zhang (2013a), Early electromagnetic waves from earthquake rupturing: I. Theoretical formulations, *Geophys. J. Int.*, *192*(3), 1288–1307.
Gao, Y., X. Chen, H. Hu, and J. Zhang (2013b), Early electromagnetic waves from earthquake rupturing: II. Validation and numerical experiments, *Geophys. J. Int.*, *192*(3), 1308–1323.
Gao, Y., X. Chen, H. Hu, J. Wen, J. Tang, and G. Fang (2014), Induced electromagnetic field by seismic waves in Earth's magnetic field, *J. Geophys. Res Solid Earth*, *119*, 5651–5685, doi:10.1002/2014JB010962.
Garambois, S., and M. Dietrich (2001), Seismoelectric wave conversions in porous media: Field measurements and transfer function analysis, *Geophysics*, *66*(5), 1417–1430.
Haartsen, M. W., and S. R. Pride (1997), Electroseismic waves from point sources in layered media, *J. Geophys. Res.*, *102*(B11), 24,745–24,769.
Hu, H., and Y. Gao (2011), Electromagnetic field generated by a finite fault due to electrokinetic effect, *J. Geophys. Res.*, *116*, B08302, doi:10.1029/2010JB007958.
Huang, Q. (2002), One possible generation mechanism of co-seismic electric signals, *Proc. Jpn. Acad., Ser. B*, *78*(7), 173–178.
Huang, Q. (2011), Retrospective investigation of geophysical data possibly associated with the M(s) 8.0 Wenchuan earthquake in Sichuan, China, *J. Asian Earth Sci.*, *41*(4–5), 421–427.
Huang, Q., H. Ren, D. Zhang, and Y. J. Zhang (2015), Medium effect on the characteristics of the coupled seismic, *Proc. Jpn. Acad., Ser. B*, *91*(1), 17–24.
Jaafar, M. Z., J. Vinogradov, and M. D. Jackson (2009), Measurement of streaming potential coupling coefficient in sandstones saturated with high salinity NaCl brine, *Geophys. Res. Lett.*, *36*, L21306, doi:10.1029/2009GL040549.
Ji, C., K. K. Choi, N. King, K. M. Larsen, and K. W. Hudnut (2004), Co-seismic slip history and early afterslip of the 2004 Parkfield earthquake, Abstract S53D-04 presented at 2004 Fall Meeting, AGU, San Francisco, Calif.
Kappler, K. (2008), Long term electromagnetic monitoring at Parkfield, CA, PhD thesis, Univ. of Calif., Berkeley.
Karakelian, D., S. L. Klemperer, A. C. Fraser-Smith, and G. A. Thompson (2002), Ultra-low frequency electromagnetic measurements associated with the 1998 Mw 5.1 San Juan Bautista, California earthquake and implications for mechanisms of electromagnetic earthquake precursors, *Tectonophysics*, *359*, 65–79.
Kim, A., and D. S. Dreger (2008), Rupture process of the 2004 Parkfield earthquake from near-fault seismic waveform and geodetic records, *J. Geophys. Res.*, *113*, B07308, doi:10.1029/2007JB005115.
Lees, J. M., and P. E. Malin (1990), Tomographic-images of P-wave velocity variation at Parkfield, California, *J. Geophys. Res.*, *95*(B13), 21,793–21,804.
Liu, P., S. Custodio, and R. J. Archuleta (2006), Kinematic inversion of the 2004 M 6.0 Parkfield earthquake including an approximation to site effects, *Bull. Seismol. Soc. Am.*, *96*(4), S143–S158.
Ma, S., S. Custodio, R. J. Archuleta, and P. Liu (2008), Dynamic modeling of the 2004 M-w 6.0 Parkfield, California, earthquake, *J. Geophys. Res.*, *113*, B02301, doi:10.1029/2007JB005216.
Matsushima, M., et al. (2002), Seismoelectromagnetic effect associated with the Izmit earthquake and its aftershocks, *Bull. Seismol. Soc. Am.*, *92*(1), 350–360.
Michelini, A., and T. V. McEvilly (1991), Seismological studies at Parkfield 1. Simultaneous inversion for velocity structure and hypocenters using cubic B-splines parameterization, *Bull. Seismol. Soc. Am.*, *81*(2), 524–552.
Okubo, K., N. Takeuchi, M. Utsugi, K. Yumoto, and Y. Sasai (2011), Direct magnetic signals from earthquake rupturing: Iwate-Miyagi earthquake of M 7.2, Japan, *Earth Planet. Sci. Lett.*, *305*(1–2), 65–72.
Pride, S. R. (1994), Governing equations for the coupled electromagnetics and acoustics of porous-media, *Phys. Rev. B*, *50*(21), 15,678–15,696.
Pride, S. R., and M. W. Haartsen (1996), Electroseismic wave properties, *J. Acoust. Soc. Am.*, *100*(3), 1301–1315.
Ren, H., Q. Huang, and X. Chen (2010), Analytical regularization of the high-frequency instability problem in numerical simulation of seismoelectric wave-fields in multi-layered porous media, *Chin. J. Geophys.-Chin. Ed.*, *53*(3), 506–511.
Ren, H., X. Chen, and Q. Huang (2012), Numerical simulation of coseismic electromagnetic fields associated with seismic waves due to finite faulting in porous media, *Geophys. J. Int.*, *188*(3), 925–944.
Ren, H., J. Wen, Q. Huang, and X. Chen (2015), Electrokinetic effect combined with surface-charge assumption: A possible generation mechanism of coseismic EM signals, *Geophys. J. Int.*, *200*(2), 835–848.
Revil, A., P. A. Pezard, and P. W. J. Glover (1999), Streaming potential in porous media 1. Theory of the zeta potential, *J. Geophys. Res.*, *104*(B9), 20,021–20,031.
Tang, J., Y. Zhan, L. F. Wang, Z. Y. Dong, G. Z. Zhao, and J. L. Xu (2010), Electromagnetic coseismic effect associated with aftershock of Wenchuan M(s) 8.0 earthquake, *Chin. J. Geophys.-Chin. Ed.*, *53*(3), 526–534.
Thurber, C., S. Roecker, K. Roberts, M. Gold, L. Powell, and K. Rittger (2003), Earthquake locations and three-dimensional fault zone structure along the creeping section of the San Andreas fault near Parkfield, CA: Preparing for SAFOD, *Geophys. Res. Lett.*, *30*(3), 1112, doi:10.1029/2002GL016004.
Thurber, C., H. J. Zhang, F. Waldhauser, J. Hardebeck, A. Michael, and D. Eberhart-Phillips (2006), Three-dimensional compressional wavespeed model, earthquake relocations, and focal mechanisms for the Parkfield, California, region, *Bull. Seismol. Soc. Am.*, *96*(4), S38–S49.
Twardzik, C., R. Madariaga, S. Das, and S. Custodio (2012), Robust features of the source process for the 2004 Parkfield, California, earthquake from strong-motion seismograms, *Geophys. J. Int.*, *191*(3), 1245–1254.
Twardzik, C., S. Das, and R. Madariaga (2014), Inversion for the physical parameters that control the source dynamics of the 2004 Parkfield earthquake, *J. Geophys. Res. Solid Earth*, *119*, 7010–7027, doi:10.1002/2014JB011238.
Ujihara, N., Y. Honkura, and Y. Ogawa (2004), Electric and magnetic field variations arising from the seismic dynamo effect for aftershocks of the M7.1 earthquake of 26 May 2003 off Miyagi Prefecture, NE Japan, *Earth Planets Space*, *56*(2), 115–123.
Wang, J., H. Hu, W. Guan, and H. Li (2015), Electrokinetic experimental study on saturated rock samples: Zeta potential and surface conductance, *Geophys. J. Int.*, *201*(2), 869–877.
Yamazaki, K. (2011), Piezomagnetic fields arising from the propagation of teleseismic waves in magnetized crust with finite conductivity, *Geophys. J. Int.*, *184*(2), 626–638, doi:10.1111/j.1365-246X.2010.04883.x.